RSC Advances

PAPER

View Article Online
View Journal | View Issue

Check for updates

Cite this: *RSC Adv.*, 2026, **16**, 1240

Fabrication of high-toughness PEDOT:PSS-based conductive hydrogel strain/temperature sensors

Jinli Zhou, *[a] Junjie Zheng,[ab] Chenxiao Wang,[a] Mengzhao Fan,[ab] Saiya Wang,[a] Fan Xiong,[a] Yunfei Li[a] and Chaoran Yang[a]

Conductive hydrogels have important potential applications in the field of flexible sensors; however, most hydrogel sensors usually possess only a single functional property. In this study, a multifunctional hydrogel with both high mechanical toughness and temperature-responsive properties was successfully constructed by introducing PEDOT:PSS into polyvinyl alcohol/sodium alginate (PVA/SA) hydrogel networks. In this study, a multifunctional conductive hydrogel with both high mechanical toughness and temperature-responsive properties was constructed by modifying PEDOT:PSS with dilute sulfuric acid and introducing it into the PVA/SA hydrogel network. The modified PEDOT:PSS significantly enhanced the electrical conductivity (48.69 mS m^{-1}), mechanical properties (fracture strength of 45.38 kPa, ductility of 209.13%) and fatigue resistance of the hydrogel through electrostatic interaction and hydrogen-bonded cross-linking. The hydrogel has excellent strain sensing ability to detect small deformation (2.5%), which is suitable for monitoring physiological signals such as joint motion, vocal cord vibration and breathing; it also has temperature response characteristics (−2.43 Ω K^{-1}, 7.91 mV K^{-1}), which can be used for body temperature monitoring. The introduction of PEDOT:PSS realizes the multifunctional sensing of hydrogel, which provides a new idea for wearable biosensors with new ideas.

Received 12th October 2025
Accepted 4th December 2025

DOI: 10.1039/d5ra07790g

rsc.li/rsc-advances

Open Access Article. Published on 02 January 2026. Downloaded on 6/16/2026 2:40:19 AM.
This article is licensed under a Creative Commons Attribution-NonCommercial 3.0 Unported Licence.

1 Introduction

In recent years, with the rapid development of wearable devices and smart sensing technologies, low-cost and high-performance multifunctional sensors are increasingly in demand in the fields of health monitoring,[1] motion tracking,[2] and human–computer interfaces.[3] However, the preparation methods of rigid materials face many challenges, such as high cost, complex preparation processes and functional limitations. Conductive hydrogel, as a flexible material, has demonstrated a wide range of potential applications in the field of sensors due to its excellent mechanical properties and biocompatibility.[4,5] Its flexible characteristics make conductive hydrogel a significant advantage in strain sensors, which can monitor the dynamic changes of the human body in real time,[6–11] such as joint movements and muscle activities. Therefore, conductive hydrogels have an important potential for application in the field of flexible sensors. Although recent reports have highlighted multimodal hydrogel sensors, achieving sensors with high toughness, low detection limits, and decoupling of temperature/strain remains a challenge.[12–14]

PVA is commonly used as a base material for hydrogels, and due to its hydrophilic hydroxyl (–OH) group, it can be physically or chemically crosslinked with a variety of compounds through hydrogen bonding to form a solid hydrogel structure.[15] Through freeze-thaw treatment[11] or cross-linking with borates,[16] PVA is able to provide a rigid scaffold for hydrogels. Meanwhile, SA is widely used in biomedical applications due to its good biocompatibility and antimicrobial properties.[17–19] SA contains a large number of carboxyl groups (–COOH) and –OH, which are able to form flexible scaffolds together with PVA through hydrogen bonding interactions as well as coordination between the carboxyl groups and the metal ions, and to enhance the flexibility of the hydrogels.[20,21] However, hydrogels prepared solely through the interaction of PVA and SA usually fail to meet the demand for high electrical conductivity. To overcome this problem, it is usually necessary to introduce conductive fillers, such as carbon-based nanomaterials, metallic nanomaterials, or conductive polymers, to enhance the conductivity of hydrogels.[22–25] Although carbon-based and metal nanomaterials excel in electrical conductivity, their high cost and poor processability limit their widespread use in practical applications. In contrast, conductive polymers, especially PEDOT:PSS, are important constituents in conductive hydrogels due to their good conductivity, flexibility, and processability.[26] PEDOT is insoluble in water, making its *in situ* incorporation into hydrogels challenging. However, PEDOT:PSS aqueous dispersions can blend and crosslink uniformly with hydrophilic networks, providing both electronic and ionic conduction channels while maintaining a high water content, making it the preferred component for conductive hydrogels. PEDOT:PSS

[a]*College of Intelligent Textile and Fabric Electronies, Zhongyuan University of Technology, Zhengzhou 450007, Henan, China. E-mail: 6684@zut.edu.cn*
[b]*Zhongwei Chemical Fiber Co., Ltd, Hebi 456750, Henan, China*

© 2026 The Author(s). Published by the Royal Society of Chemistry

Open Access Article. Published on 02 January 2026. Downloaded on 6/16/2026 2:40:19 AM. This article is licensed under a Creative Commons Attribution-NonCommercial 3.0 Unported Licence.

combines the electrical conductivity of PEDOT with the dispersibility and stability of PSS, with the sulfonic acid groups (–SO_3H) enhancing the compatibility with the hydrogel network through hydrogen bonding. In contrast, pure PEDOT requires complex modifications to disperse in aqueous systems. Therefore, PEDOT:PSS is selected for this study.[27,28]

The conductive properties of PEDOT:PSS originate from its unique molecular interaction system. The negatively charged PSS chains bind to the PEDOT conjugated backbone through electrostatic interaction, optimizing the molecular chain conformation while maintaining the charge balance and promoting the charge migration along the conjugated chain. Among them, the electrostatic attraction between PEDOT and PSS chains, the π–π stacking between PEDOT chains, and the mutual entanglement between PSS long chains work together to form an efficient charge transport network. This multilevel interaction mechanism makes PEDOT:PSS exhibit excellent electrical conductivity.[29] With the help of these three forces, PEDOT:PSS-based conductive hydrogels with high electrical conductivity, mechanical strength and uniform dispersion can be prepared. In addition, PEDOT:PSS, as a highly conductive, temperature-responsive properties,[30] is able to realize the temperature sensing function through carrier hopping.[31] Zhang *et al.*[32] prepared conductive hydrogels with the help of PVA, PEDOT:PSS and liquid metal nanoparticles, which possessed excellent self-repairing and bonding properties, and were able to realize the strain sensing with a maximum strength of 80 kPa. The PVA/PEDOT:PSS based hydrogel prepared by Yin *et al.*[33] showed a large Seebeck coefficient of 1.31 mV K^{-1}. Zhao *et al.*[34] prepared a PVA/SA/PEDOT:PSS-based hydrogel capable of multifunctional sensing for monitoring signals from strain, temperature, and electrophysiology. Chai *et al.*[35] prepared PEDOT:PSS-based hydrogels as wearable resistive sensors for breathing pattern detection.

In this study, a highly tough PVA/SA/PEDOT:PSS hydrogel (PSPSH) was prepared by cyclic freeze-thawing using PVA and SA as the main network materials of the hydrogel in combination with PEDOT:PSS. Modified by dilute sulfuric acid, PSS^+ and HSO_4^- in PEDOT:PSS were bound by electrostatic interactions, while –SO_3H formed hydrogen bonding with hydroxyl groups in PVA/SA, which significantly enhanced the electrical conductivity, mechanical toughness, and anti-fatigue properties of the hydrogel, and it was able to respond accurately under small strains PSPSH is capable of human joint movement (finger, wrist, elbow, knee), vocal cord vibration (coughing, talking), body temperature change, and respiration monitoring. In addition, the hydrogel demonstrates excellent temperature sensing capability. It demonstrates that PSPSH not only possesses excellent mechanical properties and sensing functions, but also has a wide range of application prospects, especially in the field of health monitoring and wearable devices.

2 Experimental section

2.1 Experimental materials and instruments

2.1.1 Materials. Polyvinyl alcohol-124 (PVA, AR, hydrolysis degree 98–99%, average polymerization degree 2400–2500, Xilong Scientific Co., Ltd); sodium alginate (SA, AR, viscosity 200 ± 20 mPa s, Shanghai McLean Biochemical Technology Co., Ltd); poly(3,4-ethylenedioxythiophene):poly(styrenesulfonate) (PEDOT:PSS, solid content 1.0–1.3 wt%, Shanghai McLean Biochemical Technology Co., Ltd); calcium chloride ($CaCl_2$, AR, Sinopharm Chemical Reagent Co., Ltd); sulfuric acid (H_2SO_4, AR, 98%, Guangdong Guanghua Technology Co., Ltd).

2.1.2 Characterization equipment. Field Emission Scanning Electron Microscope (SEM, Zeiss Sigma 500, Germany, equipped with GEMINI column and InLens SE detector); Fourier Transform Infrared Spectrometer (FTIR, Bruker Tensor 37e, Germany, equipped with platinum ATR attachment and diamond crystal); X-ray Diffractometer (XRD, Bruker D8 Advance, Germany, Cu Kα radiation source, $\lambda = 1.5406$ Å, LynxEye XE-T detector); X-ray Photoelectron Spectrometer (XPS, Thermo Scientific ESCALAB 250Xi, USA, Al Kα X-ray source, 1486.6 eV, spot size 500 μm).

2.1.3 Testing equipment. Electrochemical Workstation (CHI 660E, Shanghai Chenhua Instrument Co., Ltd); Digital Source Meter (Keithley 2450, Tektronix Inc., $4\frac{1}{2}$ digit resolution); Flexible Electronic Multimodal Testing System (ST600C, Suzhou, China, load sensor range 0–100 N, accuracy ±0.5%); Intelligent Constant Temperature Heating Platform (BY1010, Bangyuan, temperature control accuracy ±0.1 °C, adjustable heating rate 0–10 °C min^{-1}); Precision Electronic Balance (ME203E, Mettler-Toledo, accuracy 0.001 g); Vacuum Drying Oven (DZF-6020, Shanghai Jinghong, temperature control accuracy ±1 °C).

2.2 Preparation of PVA/SA hydrogels

1 g of polyvinyl alcohol (PVA) powder was dissolved in 9 mL of deionized water. The mixture was heated at 95 °C with magnetic stirring for 2 h until fully dissolved to obtain a 10 wt% PVA solution. 0.1 g, 0.2 g, and 0.3 g of sodium alginate (SA) powder were separately dissolved in 9.9 mL, 9.8 mL, and 9.7 mL of deionized water, respectively. Each mixture was heated at 60 °C with magnetic stirring for 2 h to prepare 1 wt%, 2 wt%, and 3 wt% SA solutions. The PVA and SA solutions were uniformly mixed at mass ratios of PVA : SA = 3 : 1, 2 : 1, 1 : 1, 1 : 2, and 1 : 3, followed by magnetic stirring for 30 min to ensure homogeneity. The mixed solution was poured into molds, frozen at −20 °C for 12 h, and subsequently thawed at room temperature (25 °C) for 6 h. This freeze-thaw cycle was repeated four times to obtain the final PVA/SA hydrogels (labeled as PSH). A pure PVA hydrogel, prepared using the same method without SA addition, was labeled as $P_{10}S_0H_0$.

2.3 Preparation of PVA/SA/PEDOT:PSS hydrogels

A 10 wt% PVA solution was homogeneously mixed with a 2 wt% SA solution according to the mass ratio PVA : SA = 3 : 1, and magnetically stirred for 30 min to ensure adequate mixing. Subsequently, 0.5 mL, 1 mL, 1.5 mL, and 2 mL of PEDOT:PSS solution were added to the mixed solution and supplemented with deionized water to make the total volume of each addition 2 mL, and stirring was continued for 30 min to ensure uniform dispersion. The mixed solution was poured into a mold and

Open Access Article. Published on 02 January 2026. Downloaded on 6/16/2026 2:40:19 AM. This article is licensed under a Creative Commons Attribution-NonCommercial 3.0 Unported Licence.

placed at −20 °C for 12 h. Subsequently, it was thawed at room temperature (25 °C) for 6 h. The freeze-thaw cycle was repeated four times to obtain the final PVA/SA/PEDOT:PSS hydrogel (denoted as PSPH). The samples were labeled as PSP_1H, PSP_2H, PSP_3H and PSP_4H according to the amount of PEDOT:PSS added.

2.4 Preparation of PVA/SA/PEDOT:PSS/H_2SO_4 hydrogels

1 mL of PEDOT:PSS solution was mixed with 1 mL of dilute sulfuric acid (6 mg mL^{-1}, 12 mg mL^{-1}, 18 mg mL^{-1}), respectively, and magnetically stirred at room temperature (25 °C) for 2 h to fully acidify PEDOT:PSS. Subsequently, the acidified PEDOT:PSS solution was added into a mixture of PVA (10 wt%) and SA (2 wt%) (PVA : SA mass ratio = 3 : 1), and magnetic stirring was continued for 30 min to ensure uniform dispersion. The mixed solution was poured into a mold and placed at −20 °C for 12 h. Subsequently, it was thawed at room temperature (25 °C) for 6 h. The freeze-thaw cycle was repeated four times to obtain a PVA/SA/PEDOT:PSS/H_2SO_4 hydrogel (noted as PSPSH). The PSPSH hydrogels were immersed in 2 w/v% $CaCl_2$ solution for 24 h to further crosslink the SA molecular chains and enhance the mechanical properties of the hydrogels. The samples were labeled as$PSPS_1H$, $PSPS_2H$ and $PSPS_3H$ according to the dilute sulfuric acid concentration.

2.5 Characterization and testing

2.5.1 Characterization part. A cold field emission scanning electron microscope (SEM, Zeiss Sigma 500, Germany) was employed to characterize the cross-sectional micromorphology and porous structure of the hydrogels. The accelerating voltage was set at 5 kV, with a working distance of 8 mm. For sample preparation, the hydrogels were frozen at −80 °C for 12 hours, followed by freeze-drying at 60 °C until fully dehydrated. The dried samples were brittle and fractured along the cross-sectional direction, then gold-coated using a Q150R ES sputter coater (Quorum, UK) with a current of 20 mA for 90 seconds. The test conditions were set at a resolution of 2.0 nm at 30 kV, with an InLens secondary electron detector and magnification ranging from 500 to 500 00×. The chemical structure of the hydrogels was analyzed by Fourier transform infrared spectroscopy (FTIR, Bruker Tensor37e, Germany), focusing on the presence of specific functional groups and dynamic covalent bonds. These were confirmed by comparing the characteristic peak position changes of monomer raw materials and reaction products. X-ray diffraction (XRD, Bruker D8 Advance, Germany) was used to assess the crystallinity and molecular chain arrangement, with conditions set at 40 kV and 40 mA, scanning from 2θ = 5–80° at a rate of 2° min^{-1} and a step size of 0.02°. X-ray photoelectron spectroscopy (XPS, Thermo Scientific ESCALAB 250Xi, USA) was used to characterize the elemental composition and chemical state of the hydrogel surface.

2.5.2 Test section. An electrochemical workstation (CHI660E, Shanghai Chenhua) was used to test the conductivity of hydrogels. Before the test, the samples were uniformly cut into rectangular samples with dimensions of 10 mm × 2 mm × 2 mm, and the excess water on the surface was gently absorbed with filter paper to ensure that the electrodes were in good contact with the samples, and in the DC mode, a voltage of 1 V was applied, and the stabilized current value (I) was recorded. The hydrogel (R) was calculated by Ohm's law:[36]

$$R = \frac{U}{I} \tag{1}$$

In eqn (1), R is the resistance of the hydrogel, Ω; U is the voltage set by the electrochemical workstation, V; and I is the stabilized current, A. The conductivity (σ) is calculated as:[37]

$$\sigma = \frac{L}{RS} \tag{2}$$

In eqn (2), L is the sample length, m; R is the sample resistance, Ω; and S is the sample cross-sectional area, m^2. Each group of samples was tested at least three times and the average value was taken to minimize the error.

The swelling properties of hydrogels were characterized by water content (M_c) and equilibrium swelling rate (E_{SR}). The hydrogel samples were immersed in deionized water and allowed to stand at room temperature (25 ± 1 °C) for 48 h to reach the swelling equilibrium. After removing the samples, excess water was gently wiped off the surface with filter paper, and the mass after swelling equilibrium (M_e) was immediately weighed and recorded. Subsequently, the samples were dried in a constant temperature drying oven (60 °C) until constant weight, and the dried mass (M_d) was recorded. The water content (M_c) and equilibrium swelling (E_{SR}) were calculated according to the following equations, respectively:[38]

$$M_c = \frac{M_w - M_d}{M_w} \times 100\% \tag{3}$$

$$E_{SR} = \frac{M_e - M_d}{M_d} \times 100\% \tag{4}$$

In eqn (3) and (4), M_c is the water content and E_{SR} is the equilibrium swelling rate. M_d is the mass of dry hydrogel, g; M_w is the mass of wet hydrogel, g, and $M_e$is the mass of hydrogel at the equilibrium of swelling, g. Each group of samples was tested at least three times and the average value was taken to minimize the error.

The mechanical properties of hydrogels were tested at 25 °C using a flexible electronic multimodal test system (ST600C, Suzhou, China). The tests were conducted at a temperature of 25 ± 1 °C and a relative humidity of 45 ± 5%. The samples were cut into rectangular specimens of 10 mm × 5 mm × 2 mm with a gauge length of 5 mm. The testing parameters were set as follows: tensile rate of 20 mm min^{-1}, preload of 0.1 N, data acquisition frequency of 50 Hz, and load cell range of 100 N (accuracy ±0.5%). $P_3S_1H_2$ samples without PEDOT:PSS were used as a control for mechanical performance. At least five parallel specimens were tested in each group. Tensile strength, elongation at break, and Young's modulus were calculated according to the ISO 37:2017 standard.[39]

© 2026 The Author(s). Published by the Royal Society of Chemistry

Open Access Article. Published on 02 January 2026. Downloaded on 6/16/2026 2:40:19 AM. This article is licensed under a Creative Commons Attribution-NonCommercial 3.0 Unported Licence.

To construct the strain and human motion sensors, the hydrogel was cut into rectangular samples with dimensions of 10 mm × 2 mm × 2 mm and the two ends of the samples were connected to the ends of a digital source meter (Keithley 2450, Tektronix Technologies Ltd). The relative resistance change rate $\left(\frac{\Delta R}{R_0}\right)$ was calculated by the following equation:[40]

$$\frac{\Delta R}{R_0} = \frac{R - R_0}{R_0} \times 100\% \quad (5)$$

In eqn (5), R_0 is the initial resistance, Ω, and R is the real-time resistance under stretching or compression, Ω. The hydrogel sheets were fixed to different joints (*e.g.*, fingers, wrists, and elbows) of the volunteers using medical tapes, and the signals of the resistance change when the joints were flexed or extended were recorded to analyze the sensor's real-time monitoring capability of the human body movement. Before testing, volunteers sat quietly for 15 minutes to stabilize their physiological state. The resting state (no movement) was used as the baseline control. Each movement was repeated 5 times, with a 2 minutes recovery interval between each test. Each set of tests was repeated at least 3 times to ensure data reliability.

To construct the temperature sensor, the hydrogel was cut into a rectangular sample with a size of 10 mm × 5 mm × 5 mm, and the top and bottom ends of the sample were connected to the electrode clips of a digital source meter (Keithley 2450, USA). The hydrogel samples were placed on a temperature-raising platform, and the temperature range was set from 15 °C to 42 °C(BY1010), with a temperature-raising rate of 0.5 °C s^{-1}. The voltage changes at different temperature differences were recorded by the digital source meter, and the temperature sensitivity (S) of the hydrogel was calculated by the following equation:[41]

$$S = \frac{\Delta V}{\Delta T} \times 100\% \quad (6)$$

In eqn (6), ΔV is the voltage change, V, and ΔT is the temperature change, °C,. Each set of tests was repeated at least 3 times and averaged to minimize error.

3 Results and discussion

3.1 Hydrogel structure design

PVA molecular chain is rich in hydroxyl group (–OH), and its linear structure forms a physical network of alternating crystalline and amorphous regions through freeze-thaw cycle, which becomes the rigid scaffold of hydrogel.[42] Carboxyl group (–COOH) and hydroxyl group (–OH) in the molecular chain of SA can form dynamic reversible physical cross-links by interacting with PVA through hydrogen bonding.[43] The density and distribution of this hydrogen bonding network directly determines the mechanical properties of the hydrogel – high-density hydrogen bonding enhances the modulus of elasticity,[44] while reversible fracture and reorganization of dynamic hydrogen bonding endows the material with a certain degree of self-repairing ability.[31] In addition, the carboxyl group of SA is partially ionized (–COO–) under alkaline conditions, which increases the network porosity through electrostatic repulsion and thus enhances the swelling performance.[45] The conjugated π-electronic structure of PEDOT confers intrinsic electrical conductivity to the hydrogel, while the sulfonic acid group (–SO_3H) of PSS is bound to the hydrogel network through hydrogen bonding. In addition, the addition of dilute sulfuric acid induces competitive binding of $PEDOT^+$ to PSS, reducing the insulating barrier effect of PSS while forming $PEDOT^+$–HSO_3^- ion pairs that significantly enhance the carrier mobility.[46] The electrical conductivity of PEDOT:PSS exhibits a negative temperature the conductivity of PEDOT:PSS exhibits a negative temperature coefficient with increasing temperature, which originates from the enhancement of the carrier thermally activated hopping mechanism.[47] Combined with the porous structure of the hydrogel, this property enables its application in temperature sensing. PEDOT:PSS is physically entangled into the PVA/SA network, and its rigid skeleton can share the external stresses and further enhance the mechanical properties. Ca^{2+} crosslinking is realized by the "egg carton" model, where two neighboring carboxylates of SA are linked to the PVA/SA network, which can be used for the temperature sensing of the carriers. The two neighboring carboxyl groups of SA form an octahedral coordination structure with Ca^{2+}, and this ionic cross-linking not only improves the network rigidity, but also enhances the fatigue resistance by restricting the molecular chain slip.[48] Notably, the degree of Ca^{2+} cross-linking can be precisely regulated by immersion time.[49–52] The structural design of the hydrogel is shown in Fig. 1.

In this study, using pure PVA hydrogel ($P_{10}S_0H_0$) as a control, we systematically investigated the effect of the PVA-to-SA mass ratio on the mechanical properties of PSH hydrogels. The results indicated that as the proportion of PVA increased, both the fracture strength and tensile stress of the PSH hydrogels exhibited an initial increase followed by a decrease, demonstrating that an appropriate amount of SA can effectively enhance the overall material performance. Mechanism analysis revealed that the incorporation of SA helps optimize the crosslinking network density, thereby improving the material's cohesion. Within a suitable SA concentration range, the hydrogel properties were significantly improved; however, excessive SA led to a reduction in tensile performance. Further investigation showed that a continuous increase in SA content resulted in the deterioration of the overall material properties, particularly when the SA concentration exceeded a critical value, beyond which both fracture strength and tensile stress decreased markedly. This can be attributed to the complete crosslinking between excess SA and PVA, whereby the inherent toughness provided by PVA was replaced by the flexibility of SA, ultimately leading to excessive softening of the material. A comprehensive evaluation of the performance indexes of the different ratios (Fig. 2a) reveals that the $P_3S_1H_2$ system exhibits an optimal combination of properties: a rupture strength of 109.68 kPa, a tensile strain of 413.65%, and an appropriate Young's modulus (33.62 kPa) and toughness (207.117 kJ m^{-3}). Combined with the multi-dimensional parameter analysis such

Open Access Article. Published on 02 January 2026. Downloaded on 6/16/2026 2:40:19 AM.
This article is licensed under a Creative Commons Attribution-NonCommercial 3.0 Unported Licence.

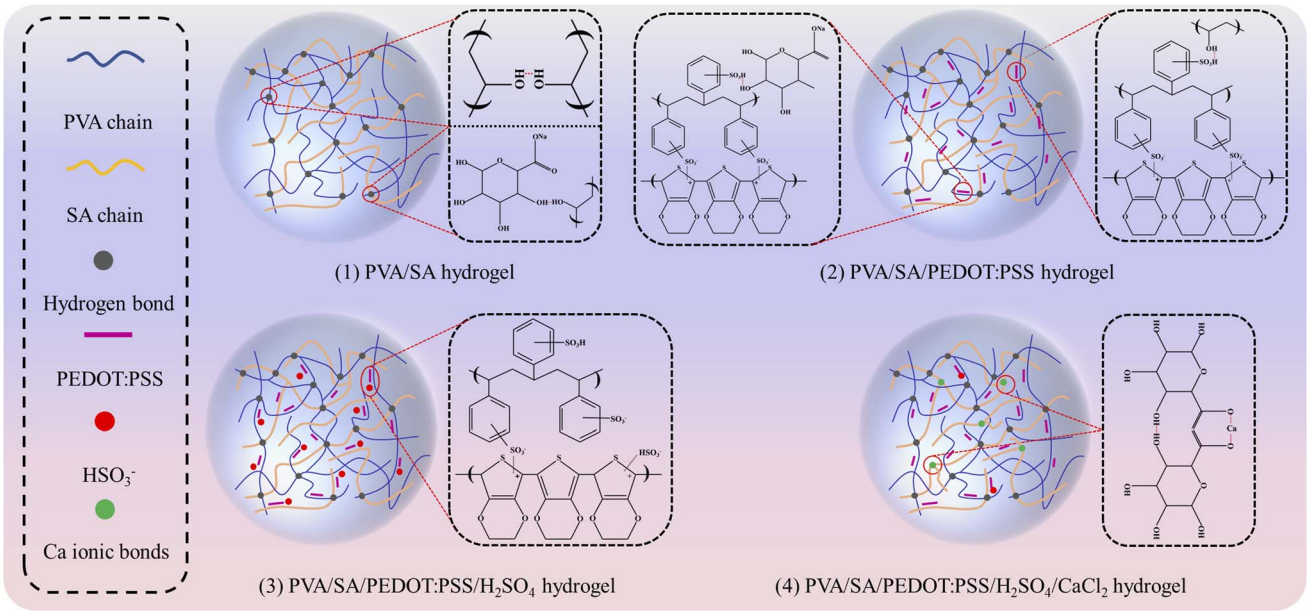

Fig. 1 Structural design of hydrogels (1) PVA/SA hydrogel (2) PVA/SA/PEDOT:PSS hydrogel (3) PVA/SA/PEDOT:PSS/H_2SO_4 hydrogel (4) PVA/SA/PEDOT:PSS/H_2SO_4/$CaCl_2$ hydrogel.

as the swelling characteristics (90.36% water content and 126.97% swelling), $P_3S_1H_2$ was finally determined as the optimum quality ratio and SA concentration ratio. The system demonstrated good deformation ability while maintaining excellent mechanical strength, providing an important reference for the development of high-performance hydrogel materials.

The synergistic modulation of PSH properties by the introduction of the conductive material PEDOT:PSS was further investigated (Table 1 for details of the experimental ratios). By comparing the control $P_3S_1P_0H_2$ without added conductive components, it was found that the introduction of PEDOT:PSS significantly improved the mechanical properties of the material. In terms of strain characteristics, $P_3S_1P_3H_2$ exhibited the

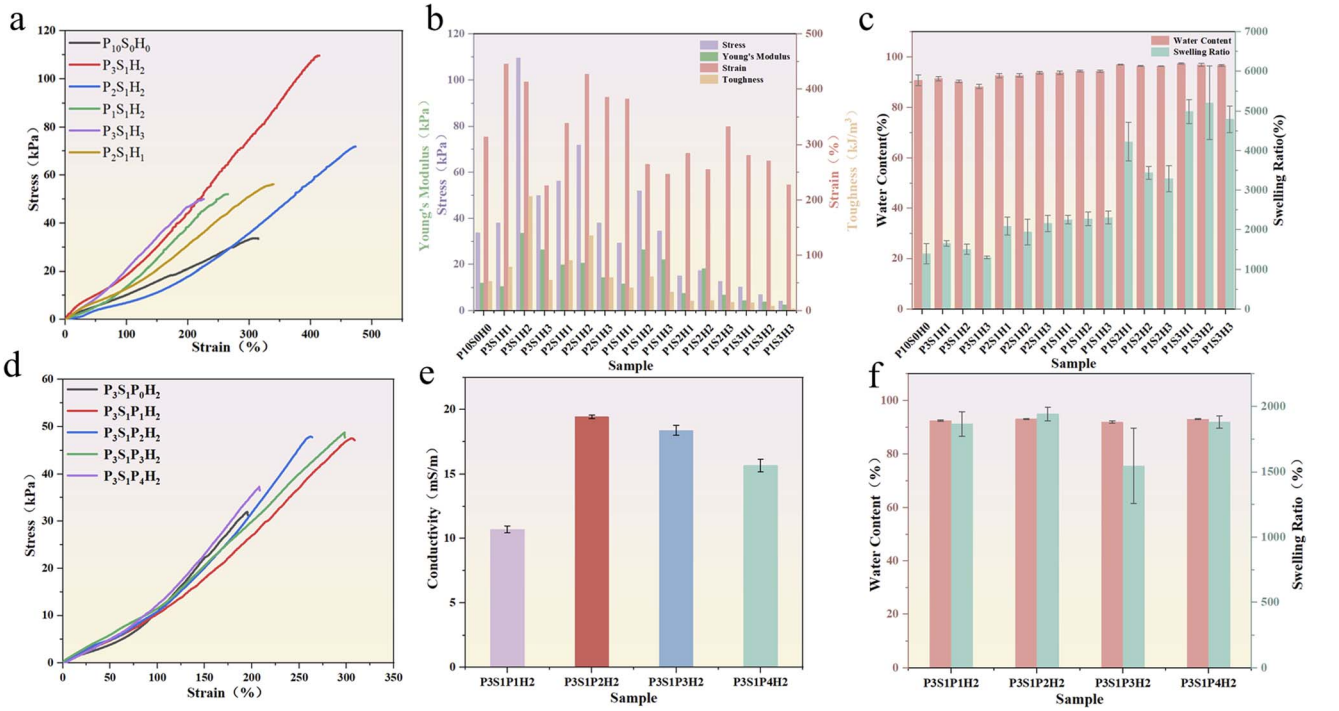

Fig. 2 (a) Tensile properties of the hydrogels; (b) summary of fracture strength, fracture strain, Young's modulus, and toughness; (c) water content and swelling ratio; (d) stress–strain curves with the incorporation of PEDOT:PSS; (e) electrical conductivity; (f) water content and swelling ratio with the incorporation of PEDOT:PSS.

© 2026 The Author(s). Published by the Royal Society of Chemistry

Open Access Article. Published on 02 January 2026. Downloaded on 6/16/2026 2:40:19 AM.
This article is licensed under a Creative Commons Attribution-NonCommercial 3.0 Unported Licence.

Table 1 Formulation table for the addition of PEDOT:PSS

Mark	PVA : SA	SA (wt%)	PEDOT:PSS (mL)	Deionized water (mL)
$P_3S_1P_0H_2$	3 : 1	2	0	2
$P_3S_1P_1H_2$	3 : 1	2	0.5	1.5
$P_3S_1P_2H_2$	3 : 1	2	1.0	1.0
$P_3S_1P_3H_2$	3 : 1	2	1.5	0.5
$P_3S_1P_4H_2$	3 : 1	2	2.0	0

optimal fracture strength (48.77 kPa), while $P_3S_1P_1H_2$ achieved the maximum tensile strain (305%). It is worth noting that the swelling and water content of the samples in each group did not show significant differences, indicating that the introduction of the conductive component did not significantly change the base swelling properties of the materials. Further analysis of the conductive properties reveals that the $P_3S_1P_2H_2$ system exhibits the optimal overall performance: it reaches a conductivity of 19.44 mS m^{-1}, while maintaining good mechanical properties (fracture strength of 47.88 kPa, strain of 262%). This phenomenon can be attributed to the fact that the addition of PEDOT:PSS in the right amount achieves a balance between the construction of the conductive network and the maintenance of the mechanical properties – the conductive pathway is not well constructed when the addition is insufficient, whereas the addition of too much may destroy the original crosslinked network structure. Based on the need for synergistic optimization, $P_3S_1P_2H_2$ was finally selected as the benchmark system for the subsequent study, which ensured a significant increase in the conductive properties while maintaining the original mechanical strength, demonstrating an ideal balance of properties.

The gradient modulation effect of dilute sulfuric acid concentration on the performance of the $P_3S_1P_2H_2$ system was then explored (Fig. 3a and b, see Table 2 for details of the ratios). Using the un-acidified treated $P_3S_1P_2S_0H_2$ as a control, the PSPSH system showed a significant structure–function evolution pattern with the elevated H_2SO_4 concentration (6 mg mL^{-1}~18 mg mL^{-1}): the fracture strength was increased from 28.14 to 36 kPa, and the conductivity jumped from 19.44 mS m^{-1} to 34.51 mS m^{-1} ($P_3S_1P_2S_3H_2$). This phenomenon is attributed to the dual mechanism of sulfuric acid: on the one hand, its protonation effect promotes the conformational transition of PEDOT:PSS molecular chain, which enhances the

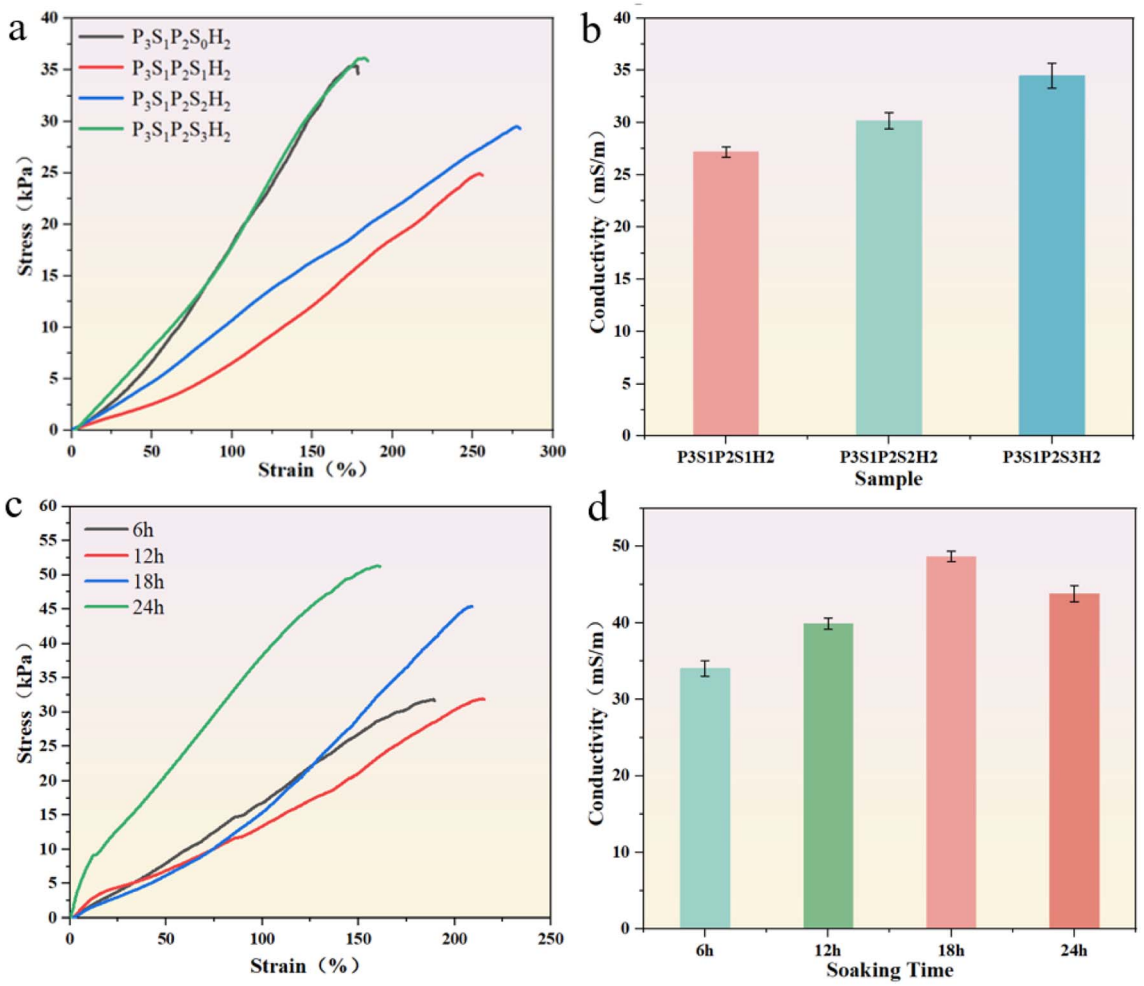

Fig. 3 (a) Stress–strain curves (b) conductivity of hydrogels with different concentrations of dilute sulfuric acid added; and (c) stress–strain curves (d) conductivity of hydrogels immersed in solutions of $CaCl_2$ for different durations.

Open Access Article. Published on 02 January 2026. Downloaded on 6/16/2026 2:40:19 AM. This article is licensed under a Creative Commons Attribution-NonCommercial 3.0 Unported Licence.

Table 2 Formulation table for the addition of H_2SO_4

Mark	PVA : SA	SA (wt%)	PEDOT:PSS (mL)	H_2SO_4 (mg mL^{-1})	H_2SO_4 (mL)	水 (mL)
$P_3S_1P_2S_0H_2$	3 : 1	2	1.0	0	0	1
$P_3S_1P_2S_1H_2$	3 : 1	2	1.0	6	1.0	0
$P_3S_1P_2S_2H_2$	3 : 1	2	1.0	12	1.0	0
$P_3S_1P_2S_3H_2$	3 : 1	2	1.0	18	1.0	0

continuity of the conductive pathway through the planarization and reconstruction of benzene ring; on the other hand, the excessive acid concentration (18 mg mL^{-1}) leads to the over-densification of the crosslinked network, which results in the decrease of the tensile strain from 262% to 198%, and exhibits the typical strength-ductility trade-off effect. Based on the principle of performance balance, the moderately acidified strength system $P_3S_1P_2S_2H_2$ (breaking strength of 32.45 kPa, conductivity of 28.76 mS m^{-1}, and strain of 235%) was selected as the substrate for subsequent optimization.

Further studies on the modulation law of $CaCl_2$ crosslinking aging (2% w/v solution, 6–24 h) on the material properties (Fig. 3c and d) revealed that the immersion time was positively correlated with the crosslinking density: the performance threshold was reached at 18 h, at which time Ca^{2+} formed an optimal coordination network with carboxyl groups of SA to achieve a synergistic enhancement of strength-conductivity and obtain the breakthrough performance parameters were 209.13% tensile strength, 45.38 kPa breaking strength (38.6% increase from the unsoaked system), and 48.69 mS m^{-1} conductivity (2.5 times increase from the initial value). The optimized process successfully breaks through the technical bottleneck of traditional hydrogel's high strength and high conductivity by regulating the ion cross-linking density and proton doping level step by step (Table 3).

3.2 Analysis of characterization results

In this study, the PSPSH system was systematically structurally characterized by XRD, XPS, FTIR, and SEM techniques. XPS full spectrum analysis showed that the sample surface was mainly composed of five elements, C (63.11 at%), O (27.17 at%), Cl (2.79 at%), Ca (1.54 at%), and Na (0.63 at%) (Fig. 4a). The high-resolution C 1s spectrum can be fitted to three characteristic peaks of 284.6 eV (C–C/C–H), 286.0 eV (C–O) and 288.8 eV (COOH) (Fig. 4b), whereas the Ca 2p spectrum shows a bimodal structure of 347.0 eV ($2p_{3/2}$) and 350.5 eV ($2p_{1/2}$), with spin–orbit splitting energy of 3.5 eV (Fig. 4c). It is noteworthy that the surface exhibits significant carbon enrichment (O/C ratio of 0.43) and the Ca/Cl atomic ratio (0.55) is in good agreement with the theoretical value of $CaCl_2$ (0.5). The ionic crosslinking efficiency was quantitatively calculated to be 91%. In particular, the Ca 2p binding energy was negatively shifted by 0.5 eV compared to free $CaCl_2$, a feature that confirms the coordination between Ca^{2+} and the carboxyl groups of sodium alginate, restricting polymer chain segment mobility, providing direct evidence for the cross-linking mechanism of the hydrogel. O 1s spectra showed characteristic peaks at 531.8 eV (OH^-) and 529 eV (O^{2-}) indicating the presence of hydroxyl and oxide fractions on the surface of the sample (Fig. 4d).

The XRD pattern (Fig. 4e) showed three characteristic diffraction peaks at 19.6°, 31.3° and 40.8°.The diffraction peak at 19.6° mainly originates from the amorphous structure of PVA and sodium alginate, which suggests that the hydrogel matrix is predominantly amorphous. The weak diffraction peak at 31.3° corresponds to the (200) crystalline plane of anhydrous $CaCl_2$, and its lower peak intensity suggests that most of the Ca^{2+} ions are involved in the cross-linking reaction with the carboxyl group (–COO–) of sodium alginate, forming an amorphous cross-linked network structure. This result is corroborated with the non-detection of the diffraction peak at 45.2° (the (220) crystal plane of anhydrous $CaCl_2$), which further confirms that Ca^{2+} exists predominantly in a ligandic form. The diffraction peak at 40.8° is attributed to the (101) crystal plane of the pure PVA, which suggests that part of the crystalline region of PVA still exists in the system.

The molecular structure of the PVA/SA/PEDOT:PSS composite hydrogels was systematically analyzed by FTIR spectroscopy to characterize the molecular structure of the composite hydrogels (Fig. 4f and g). Spectroscopic analysis showed that the broad absorption peak at 3430 cm^{-1} was attributed to the stretching vibration of the hydroxyl group (–

Table 3 Summary of advanced conductive hydrogel sensors and performance

Materials	Stretchability (%)	Fracture Strength (kPa)	Sensitivity (GF)	Ref.
CS/SA/PMIA	48%	16.8	—	53
AA/SBMA/LMA	176%	158	1.23/1.32	54
PVA/Ca/CNT	100%	110	4.5/11.1	55
PAAm/PEDOT:PSS	1000%	190	1.67	56
CNF/PVA/PEDOT:PSS	926%	36.82	—	57
PVA/NaCl/GO	180%	65	74.18	58
PVA/SA/PEDOT:PSS	209.13%	45.38	0.46/0.57	This work

© 2026 The Author(s). Published by the Royal Society of Chemistry

Open Access Article. Published on 02 January 2026. Downloaded on 6/16/2026 2:40:19 AM.
This article is licensed under a Creative Commons Attribution-NonCommercial 3.0 Unported Licence.

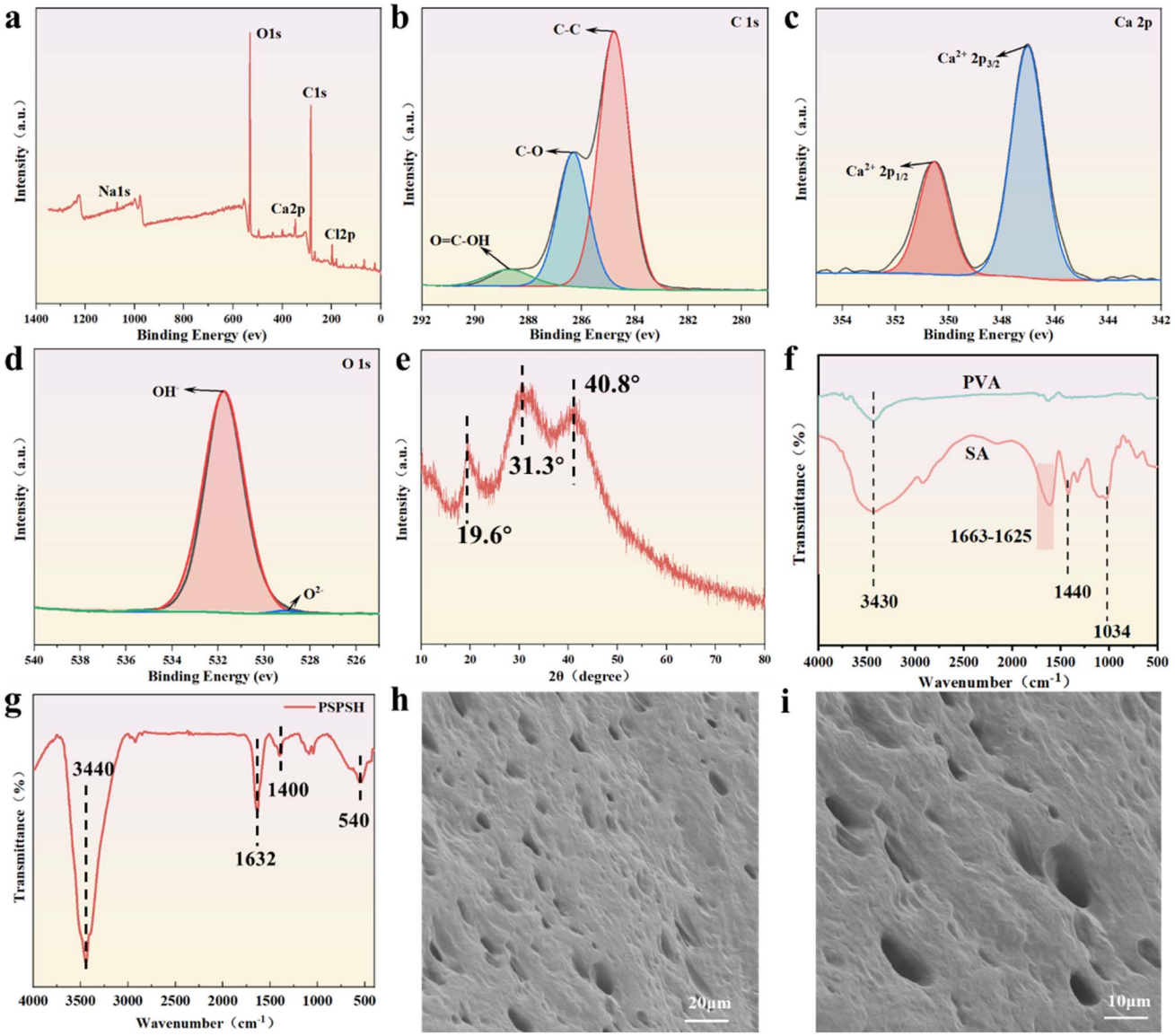

Fig. 4 Characterization (a) XPS total spectrum (b) C 1s (c) Ca 2p (d) O 1s (e) XRD (f) FTIR (PVA, SA) (g) FTIR (PSPSH) (h) PSPSH surface SEM (i) PSPSH cross section SEM.

OH) in PVA and SA, and the peak was shifted to 3400 cm^{-1} in the PSPSH composite system, confirming the formation of a complex hydrogen-bonding network between PVA hydroxyl, SA carboxylate, and PSS sulfonate groups. This structural feature is directly associated with the excellent solvation properties and mechanical strength of the material. It is particularly noteworthy that the vibrational peak of the carboxylate in the composite system is shifted to 1632 cm^{-1} compared with the characteristic peak of pure SA at 1625 cm^{-1}, and this redshift of 7 cm^{-1} clearly reveals that there are significant intermolecular interactions between SA, PVA and PEDOT components. Interactions between SA and the PVA and PEDOT components. In addition, the low-frequency vibrational signal at 540 cm^{-1} may originate from the out-of-plane deformation vibration of the PEDOT thiophene ring or metal–ligand interactions, which provides an important basis for elucidating the conductive mechanism of the material. These FTIR analysis results corroborate with the previous XPS and XRD characterizations, and together reveal the multiscale structural features of the hydrogel system, including the surface chemical composition, the dispersed PVA microcrystalline regions in the bulk amorphous matrix, and the three-dimensional network structure constructed by hydrogen bonding and ligand bonding. This unique structural design provides an important theoretical basis for the development of hydrogel materials with controllable performance and multifunctional properties. SEM images show that PSPSH exhibits more pore structure features (Fig. 4h and i). Which directly correlates with the macroscopically observed low mechanical hysteresis and stable resistance signal. This pore structure morphology may be closely related to its excellent mechanical properties and stable electrical characteristics.

© 2026 The Author(s). Published by the Royal Society of Chemistry

Open Access Article. Published on 02 January 2026. Downloaded on 6/16/2026 2:40:19 AM.
This article is licensed under a Creative Commons Attribution-NonCommercial 3.0 Unported Licence.

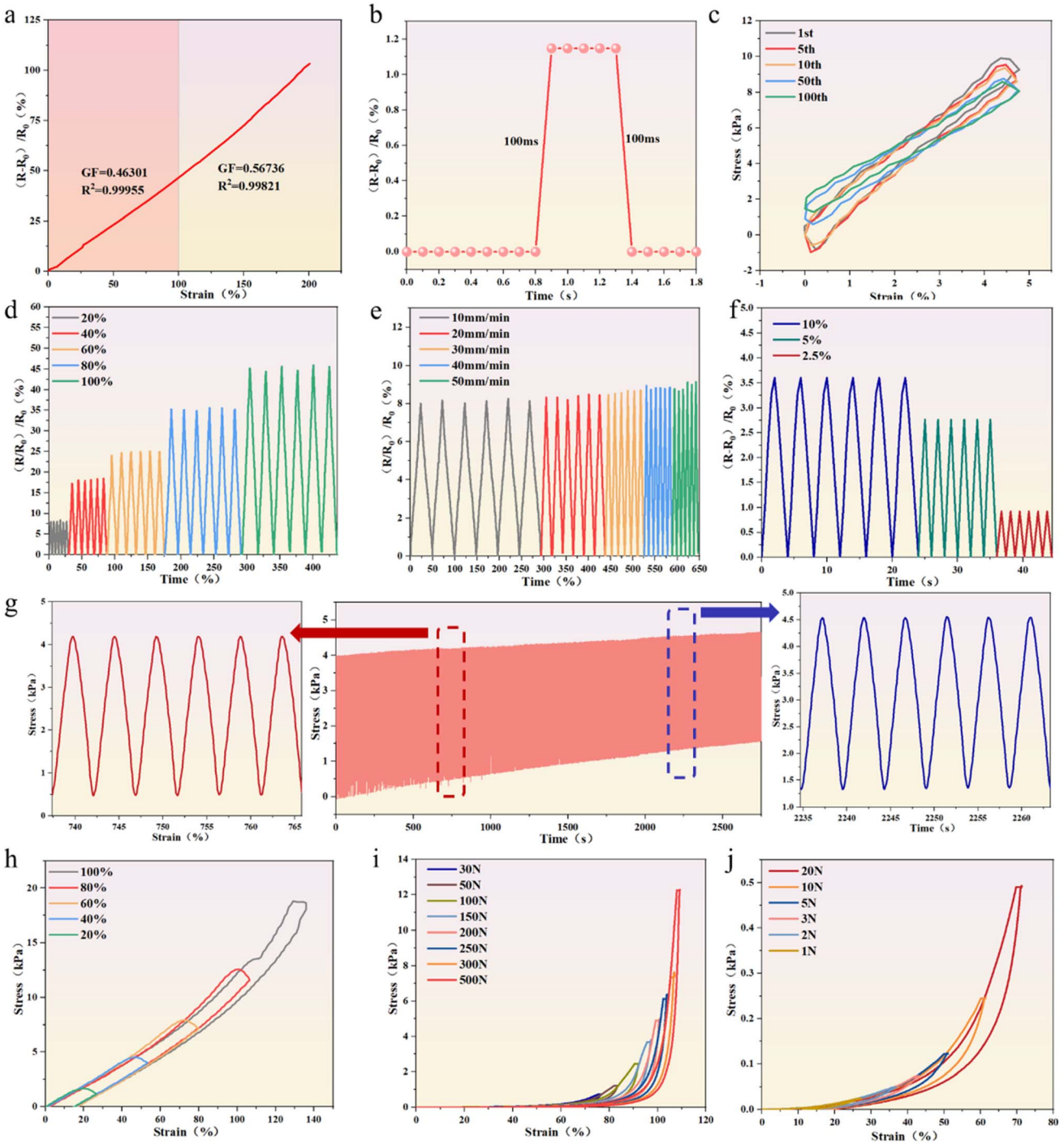

Fig. 5 Strain sensing characteristics of hydrogel (a) fitting curve (sensitivity) (b) response and recovery time (c) hysteresis, 20% strain (d) resistance change at different strains (20 mm min^{-1}) (e) resistance change at different velocities (20% strain) (f) resistance change at small strains, the lowest strain that can be detected is 2.5% (g) stability of the force value for 500 cycles (20%) (h) tensile loading–unloading curves (i) compression loading–unloading curves under compression force values of 30 N–500 N (j) compression loading–unloading curves under compression force values of 1 N–20 N.

3.3 Strain sensing

The strain sensing properties of PVA/SA/PEDOT:PSS ternary composite hydrogel were revealed (Fig. 5). The material exhibits excellent linear response properties over a wide strain range of 0–200%, and its sensitivity shows strain-dependent characteristics: the sensitivity factor (GF) is 0.46 in the 0–100% interval, and it is enhanced to 0.57 in the 100–200% interval (Fig. 5a). The dynamic response test shows that the response time and recovery time of the material to 10% step strain under 100 mm min^{-1} tensile rate are both in the order of 100 ms (Fig. 5b), and the hysteresis return line remains basically stable after 100 cycles of loading, which confirms its reliable sensing

© 2026 The Author(s). Published by the Royal Society of Chemistry

Open Access Article. Published on 02 January 2026. Downloaded on 6/16/2026 2:40:19 AM.
This article is licensed under a Creative Commons Attribution-NonCommercial 3.0 Unported Licence.

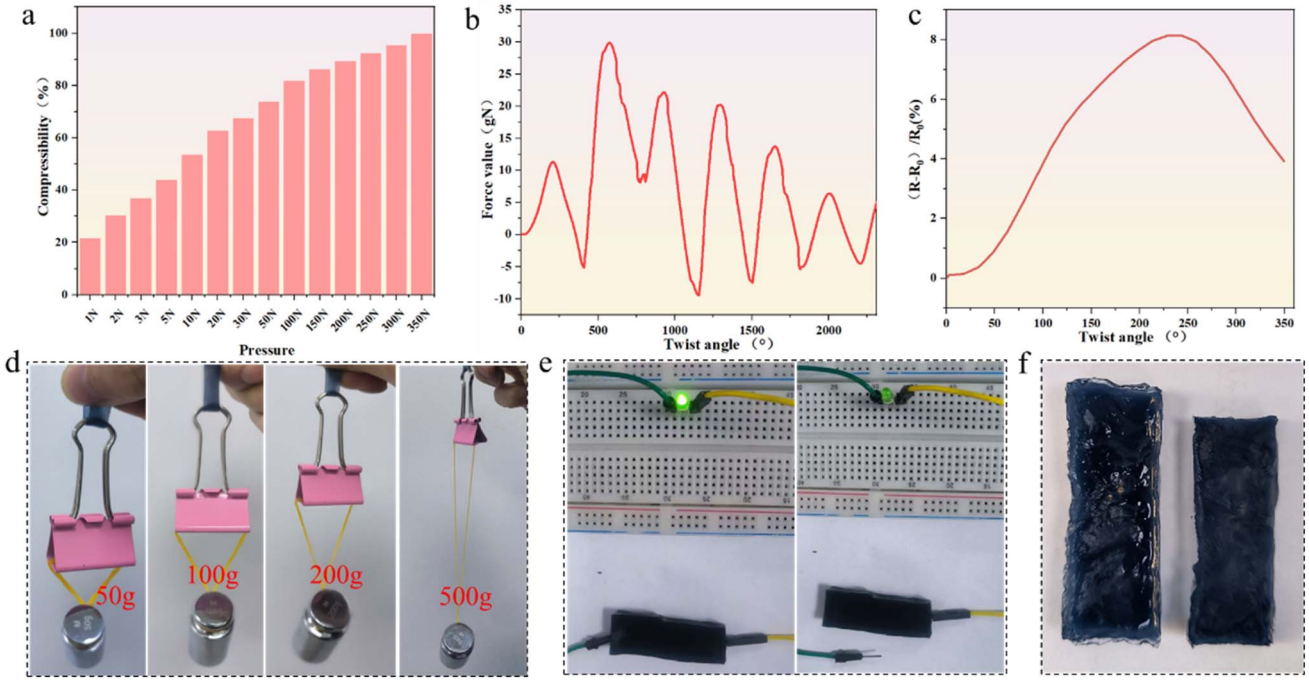

Fig. 6 (a) Histogram of pressure and compression rate (b) torsion angle–force relationship (c) torsion angle–resistance relationship (d) optical image of hydrogel load-bearing, which can lift up to 500 g weights (e) LED light that can be illuminated as a conductor (f) optical image of PSPSH (left) and after 30 days of placement.

repeatability (Fig. 5c). Further multi-dimensional performance validation reveals that the material resistivity change rate basically does not fluctuate under different applied strains (10–100%) (Fig. 5d), and the resistivity change rate basically remains flat (8%) under different loading rates (10–50 mm min^{-1}) (Fig. 5e), and its strain detection threshold is as low as 2.5% (Fig. 5f). Notably, PSPSH maintains stable resistance response after 500 cycles of loading (Fig. 5g), with a stress decay rate of less than 11.76%, demonstrating excellent fatigue resistance. This performance is attributed to the synergistic energy-dissipation mechanism between the Ca^{2+} crosslinked network and the PVA crystalline regions.[59,60] Mechanical test data show that the material has an elastic recovery stress of 17.5 kPa at 100% tensile strain (Fig. 5h), can withstand 500 N load in compression mode and generate a compressive stress of 12.5 kPa, which can be detected as low as 1 N load (Fig. 5i and j), and the compression rate increases with the increase of pressure (Fig. 6a). This strong property originates from the synergistic energy dissipation mechanism between the crystalline regions of PVA and the SA-Ca^{2+} ionic crosslinking network.

Innovatively, the study extends the mechanical-electrical coupled sensing of the material, confirming its 3D deformation sensing capability (Fig. 6b and c). Application validation experiments show that the hydrogel can stably carry a 500 g weight (breaking strength > 45 kPa) (Fig. 6d) and act as a flexible conductor to drive LED circuits (Fig. 6e), and the PSPSH is compared with the optical image after 30 days of placement (at 6 °C/45% humidity), and its adjustable conductivity range of 19.44∼48.69 mS m^{-1} is highly matched with the electrical characteristics of the human tissue. Properties are highly matched, laying a material foundation for the development of a new generation of bioelectronic interface devices. The fulfillment of both strain and temperature sensing functions lays the material foundation for developing next-generation bioelectronic interface devices.

3.4 Temperature sensing

The temperature sensing properties of PEDOT:PSS arise from the enhanced thermally stimulated carrier hopping and tunneling effects. Its resistance decreases with increasing temperature (negative temperature coefficient), while the voltage response is attributed to the Seebeck effect. The distinct PVA crystalline peaks in the XRD pattern reveal the presence of ordered crystalline domains that serve as physical crosslinking points. The intensified thermal vibrations of these regions at elevated temperatures indirectly modulate carrier scattering within the PEDOT:PSS conductive pathways, thereby contributing to the observed negative temperature coefficient (NTC) effect. The temperature sensing properties of PEDOT:PSS arise from the enhanced carrier hopping and tunneling effects within individual grains and between neighboring nanosheets under thermal stimulation.[17] At room temperature, the charge carrier mobility in PEDOT:PSS composites is relatively limited. However, as the temperature increases, electrons in the valence band are excited and jump to the conduction band, leading to an increase in conductivity.[61,62] In addition, in PEDOT:PSS materials, the movement of carriers from the hot end to the cold end creates a potential difference, resulting in a reverse flow of charge. When the thermal movement of charges reaches a dynamic equilibrium with the internal electric field, a stable

© 2026 The Author(s). Published by the Royal Society of Chemistry

Open Access Article. Published on 02 January 2026. Downloaded on 6/16/2026 2:40:19 AM.
This article is licensed under a Creative Commons Attribution-NonCommercial 3.0 Unported Licence.

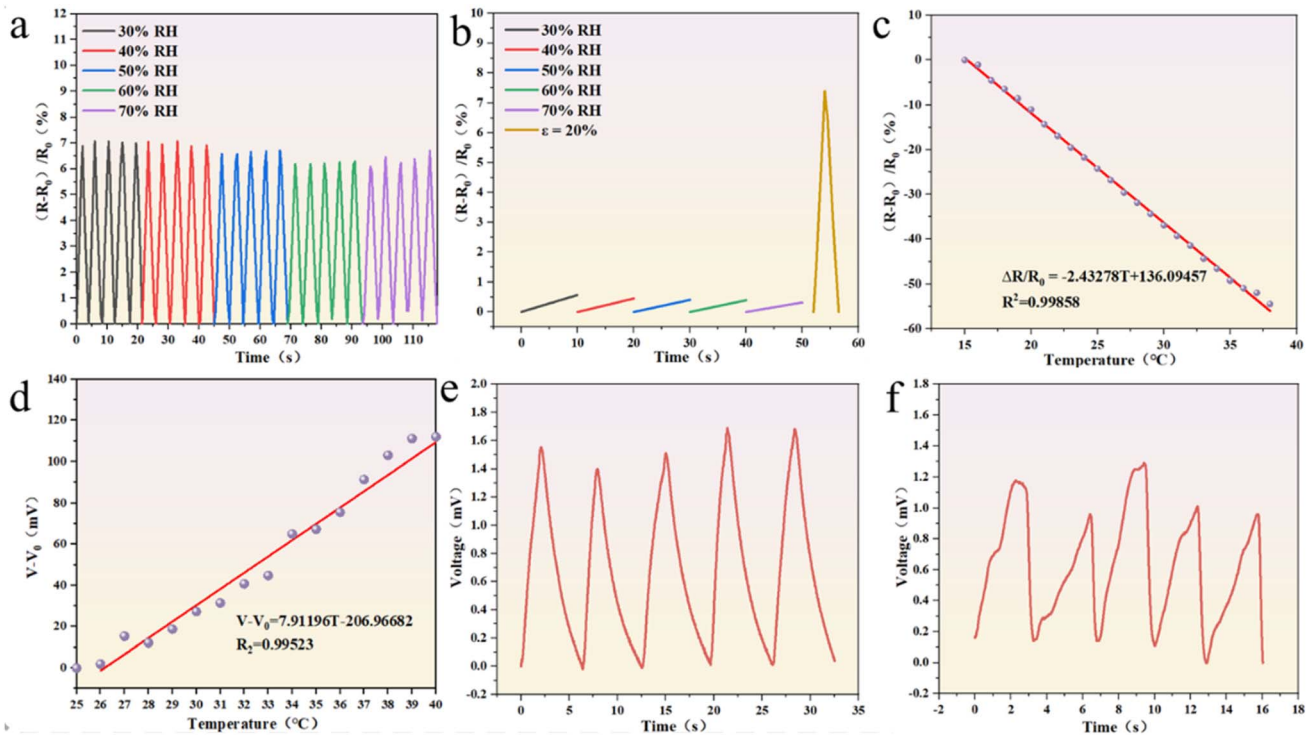

Fig. 7 Temperature sensing characteristics of PSPSH (a) resistance change at different humidity and 20% stretch (b) resistance change at different humidity in static condition (c) resistance–temperature correlation curves (d) voltage–temperature correlation curves (e) voltage change at the touch of a finger (f) voltage change in breathing condition.

thermal potential is established.[63] Based on these mechanisms, two types of temperature sensors have been developed using PSPSH: resistance-responsive and voltage-responsive sensors. As shown in Fig. 8c and d, the resistance monotonically decreases with increasing temperature difference, while the voltage monotonically increases. The sensitivity coefficients of these two sensors are $-2.43\ \Omega\ K^{-1}$ and $7.91\ mV\ K^{-1}$, respectively. These sensors exhibit stable cycling performance and can output consistent voltage signals under different temperature gradients, showing excellent thermal response stability. Not only that, the PSPSH was insensitive to the cycling resistance change under different humidity at 20% strain as shown in Fig. 7a, moreover, the resistance change when the hydrogel was stationary at different humidity was also very small (Fig. 7b), indicating that the hydrogel was insensitive to humidity. After that the temperature change produced at the moment of touching the hydrogel using a finger was tested and the voltage change was recorded as shown in Fig. 7e. It was also possible to monitor the change in the voltage signal during the breathing state, as there is exhalation and inhalation in the breathing process, thus generating a change in temperature, which in turn generates a voltage signal. These results highlight the potential of PSPSH for temperature sensing applications.

3.5 Human motion sensing

In this study, we systematically validated the pervasive application of PVA/SA/PEDOT:PSS hydrogel sensors for multi-scale biomechanical monitoring of the human body (Fig. 8), and successfully realized the full-dimensional biosignal capture from macroscopic joint motion (>50% strain) to micro-expressive muscle movement (<5% strain). For macro-motion monitoring, by integrating the sensors into biomechanical nodes such as finger joints (Fig. 8e), wrist joints (Fig. 8f), elbow joints (Fig. 8d), and knee joints (Fig. 8g), it was found that the rate of change of the electrical resistance showed a strong linear correlation with the bending angle of the joints. Especially in the dynamic monitoring of the finger joints, the sensor can realize the accurate recognition of 0–90° bending range. In the microstrain sensing dimension, the laryngeal bio-vibration monitoring model was innovatively developed (Fig. 8b and c). Through the submicron deformation (<5% strain) triggered by vocal fold vibration, the sensor successfully captured the differentiated waveform characteristics of specific phonemes such as *Z*, *U*, *T*, *etc.*, and could clearly distinguish the onset phases of consecutive syllables. In cough monitoring, the sensor not only detects a single coughing event, but also quantitatively evaluates the cough intensity grading through the rate of change of peak resistance (0.1–0.25%). Notably, the sensor breaks through the technical bottleneck of traditional flexible devices in micro-expression recognition: it realizes the feature extraction of smiling expression through the detection of small contraction strain of 0.1–0.25% in facial muscles (Fig. 8a). In the field of sports medicine, through arm muscle tremor monitoring experiments, the sensor can recognize muscle fiber activation patterns in the lower frequency range, providing a new method for sports rehabilitation assessment. To further evaluate the signal interference between strain and

© 2026 The Author(s). Published by the Royal Society of Chemistry

Open Access Article. Published on 02 January 2026. Downloaded on 6/16/2026 2:40:19 AM.
This article is licensed under a Creative Commons Attribution-NonCommercial 3.0 Unported Licence.

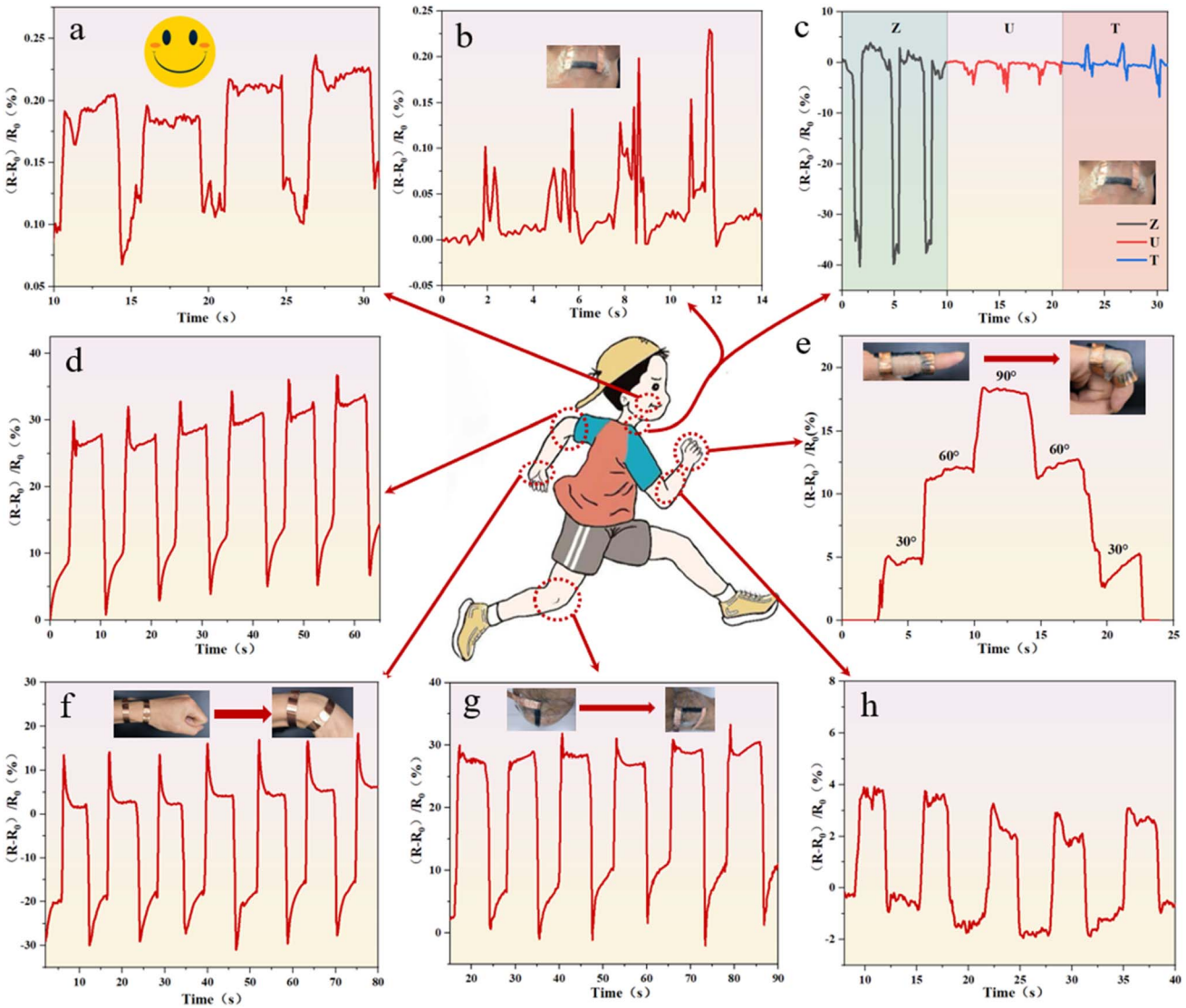

Fig. 8 PSPSH enables monitoring of joint movements (finger, wrist, elbow, knee) and small strains (a) smile (b) cough (c) vocalization (*Z*, *U*, *T*) (d) elbow (e) finger (f) wrist (g) knee (h) arm muscles.

temperature sensing, we designed a coupled experiment. The results show that at 20% strain, the resistance change rate induced by temperature is less than 3%, indicating that PSPSH exhibits good signal decoupling ability. This is mainly attributed to the stability of the conductive pathways of PEDOT:PSS and the mechanical buffering effect of the PVA/SA network, providing innovative solutions for cutting-edge fields such as intelligent prosthetic limb control, speech impediment assistance and neurodegenerative disease monitoring. We acknowledge the limitations of current humidity testing and pledge to conduct in-depth evaluations under more realistic wearable conditions, such as simulated sweat and dynamic humidity variations, in subsequent studies.

4 Conclusion

In this study, a new conductive hydrogel material was designed and prepared by introducing PEDOT:PSS into the PVA/SA hydrogel network. By adding PEDOT:PSS and modifying it by dilute sulfuric acid, hydrogen bonding and electronic interactions were formed between PEDOT:PSS and PVA/SA chains, which endowed the hydrogel with excellent toughness (fracture strength of 45.38 kPa and ductility of 209.13%) and conductivity (conductivity of 48.69 mS m^{-1}). This strategy not only improves the physical properties of the hydrogel, but also enables it to exhibit excellent durability under stress. The hydrogel is highly sensitive to both small (2.5%) and large strains (more than 100%). It not only senses joint flexion in human movement, but also accurately converts small muscle changes, expression changes, coughing and talking, and other small movements into measurable electrical signals. Therefore, the hydrogel it demonstrates potential for applications in health monitoring, providing a proof-of-principle for future more complex applied research, while acknowledging there remains a gap to final clinical or practical application. In addition, the hydrogel has high sensitivity to temperature changes (−2.43 Ω K^{-1} and

Open Access Article. Published on 02 January 2026. Downloaded on 6/16/2026 2:40:19 AM. This article is licensed under a Creative Commons Attribution-NonCommercial 3.0 Unported Licence.

7.91 mV K^{-1}). It can sense movements such as touch and breathing into measurable electrical signals. Therefore, the hydrogel can be widely used in the field of wearable temperature sensors for respiration monitoring. This study not only provides a new approach for the design of conductive hydrogels, but also opens up a new direction for the development of multifunctional wearable sensors, which is of great scientific significance and application value.

Ethical statement

Informed consent was obtained for all experiments involving human volunteers.

Conflicts of interest

There are no conflicts to declare.

Data availability

The data supporting this article have been included as part of the supplementary information (SI). Supplementary information is available. See DOI: https://doi.org/10.1039/d5ra07790g.

Acknowledgements

This work was supported by the Henan Province Science and Technology Key Research Project (Project No. 252102230012, 252102211104); China Textile Industry Federation Science and Technology Guidance Program Project (Project No. 2025042); Zhong yuan University of Technology Natural Science Foundation Project (Project No. K2025YB017); Henan Province Functional Textile Materials Key Laboratory Open Research Fund (Project No. HNFZ2024014); Zhongyuan University of Technology Graduate Research Innovation Program (Project No. YKY2025ZK32).

References

1 J. Li, Z. Fang, D. Wei, *et al.*, Flexible pressure, humidity, and temperature sensors for human health monitoring, *Adv. Healthcare Mater.*, 2024, **13**(31), 2401532.
2 B. S. Priyadarshini, R. Mitra and U. Manju, Titania nanoparticle-stimulated ultralow frequency detection and high-pass filter behavior of a flexible piezoelectric nanogenerator: a self-sustaining energy harvester for active motion tracking, *ACS Appl. Mater. Interfaces*, 2023, **15**(39), 45812–45822.
3 D. Ruan, G. Chen, X. Luo, *et al.*, Bionic octopus-like flexible three-dimensional force sensor for meticulous handwriting recognition in human-computer interactions, *Nano Energy*, 2024, **123**, 109357.
4 N. Hasan, M. M. Bhuyan and J. H. Jeong, Single/Multi-Network Conductive Hydrogels—A Review, *Polymers*, 2024, **16**(14), 2030.
5 K. B. C. Imani, J. M. Dodda, J. Yoon, *et al.*, Seamless integration of conducting hydrogels in daily life: from preparation to wearable application, *Adv. Sci.*, 2024, **11**(13), 2306784.
6 Z. Zhao, J. Liu, J. Lv, *et al.*, Facile One-Pot Preparation of Polypyrrole-Incorporated Conductive Hydrogels for Human Motion Sensing, *Sensors*, 2024, **24**(17), 5814.
7 C. Ji, Y. Wang, Q. Qi, *et al.*, Electrically Conductive Hydrogels for Flexible Wearable Devices: Materials, Design, and Applications, *Adv. Mater. Technol.*, 2025, e01044.
8 R. Qi, X. Zhi, X. Xu, *et al.*, Conductive hydrogels: Synergistic optimization of structure-property-application in wearable sensors, *Mater. Today Chem.*, 2025, **48**, 102936.
9 F. Han, S. Chen, F. Wang, *et al.*, High-Conductivity, Self-Healing, and Adhesive Ionic Hydrogels for Health Monitoring and Human-Machine Interactions Under Extreme Cold Conditions, *Adv. Sci.*, 2025, **12**(16), 2412726.
10 J. Sun, W. Dai, Q. Guo, *et al.*, Self-powered wearable electrochemical sensor based on composite conductive hydrogel medium for detection of lactate in human sweat, *Biosens. Bioelectron.*, 2025, **277**, 117303.
11 X. Hu, Z. Liu and Y. Zhang, Three-Dimensionally Architected Tactile Electronic Skins, *ACS Nano*, 2025, **19**(15), 14523–14539.
12 P. Wang, G. Wang, G. Sun, *et al.*, A flexible-integrated multimodal hydrogel-based sensing patch, *Nano-Micro Lett.*, 2025, **17**(1), 1–19.
13 M. Wu, C. Qiao, P. F. Sui, *et al.*, Stratum Corneum-Inspired Zwitterionic Hydrogels with Intrinsic Water Retention and Anti-Freezing Properties for Intelligent Flexible Sensors, *Adv. Funct. Mater.*, 2025, 2422755.
14 Y. Li, X. Yang, Y. Ding, *et al.*, A Wireless Health Monitoring System Accomplishing Bimodal Decoupling Based on an "IS"-Shaped Multifunctional Conductive Hydrogel, *Small*, 2025, **21**(21), 2411046.
15 X. Liang, H. J. Zhong, H. Ding, *et al.*, Polyvinyl alcohol (PVA)-based hydrogels: Recent progress in fabrication, properties, and multifunctional applications, *Polymers*, 2024, **16**(19), 2755.
16 H. Adelnia, R. Ensandoost, S. S. Moonshi, *et al.*, Freeze/thawed polyvinyl alcohol hydrogels: Present, past and future, *Eur. Polym. J.*, 2022, **164**, 110974.
17 M. Li, Y. Wang, Q. Wei, *et al.*, A high-stretching, rapid-self-healing, and printable composite hydrogel based on poly (vinyl alcohol), nanocellulose, and sodium alginate, *Gels*, 2024, **10**(4), 258.
18 H. Liu, Y. Li, Q. Sun, *et al.*, Triboelectric wearable devices for accelerated wound healing, *Chem. Eng. J.*, 2024, **497**, 154628.
19 F. Han, T. Wang, G. Liu, *et al.*, Materials with tunable optical properties for wearable epidermal sensing in health monitoring, *Adv. Mater.*, 2022, **34**(26), 2109055.
20 N. S. El-Sayed, A. H. Hashem, T. A. Khattab, *et al.*, New antibacterial hydrogels based on sodium alginate, *Int. J. Biol. Macromol.*, 2023, **248**, 125872.
21 X. Jiang, N. Xiang, H. Zhang, *et al.*, Preparation and characterization of poly (vinyl alcohol)/sodium alginate hydrogel with high toughness and electric conductivity, *Carbohydr. Polym.*, 2018, **186**, 377–383.

© 2026 The Author(s). Published by the Royal Society of Chemistry

Open Access Article. Published on 02 January 2026. Downloaded on 6/16/2026 2:40:19 AM. This article is licensed under a Creative Commons Attribution-NonCommercial 3.0 Unported Licence.

22 Y. Dong, Z. Gao, Q. Mi, *et al.*, Highly sensitive and structure stable polyvinyl alcohol hydrogel sensor with tailored free water fraction and multiple networks by reinforcement of conductive nanocellulose, *Int. J. Biol. Macromol.*, 2024, **281**, 136128.
23 H. Ding, Y. Gu, Y. Ren, *et al.*, The latest research progress of conductive hydrogels in the field of electrophysiological signal acquisition, *J. Mater. Chem. C*, 2024, **12**(9), 3030–3052.
24 K. Mahato, T. Saha, S. Ding, *et al.*, Hybrid multimodal wearable sensors for comprehensive health monitoring, *Nat. Electron.*, 2024, **7**(9), 735–750.
25 L. Hu, S. Azhari, H. Zhang, *et al.*, MXene-Integrated Contact Lens: A Breakthrough in Wearable Eye Protection and Healthcare, *Small Sci.*, 2025, 2400628.
26 F. Han, P. Ge, F. Wang, *et al.*, Smart contact Lenses: From rational design strategies to wearable health monitoring, *Chem. Eng. J.*, 2024, **497**, 154823.
27 R. Wan, S. Liu, Z. Li, *et al.*, 3D printing of highly conductive and strongly adhesive PEDOT:PSS hydrogel-based bioelectronic interface for accurate electromyography monitoring, *J. Colloid Interface Sci.*, 2025, **677**, 198–207.
28 B. Zhao, Z. Li, L. Zheng, *et al.*, Recent progress in the biomedical application of PEDOT:PSS hydrogels, *Chin. Chem. Lett.*, 2024, **35**(10), 109810.
29 Z. W. Lin, Y. L. Chen, W. L. Lei, *et al.*, Hierarchically structured conductive hydrogels for electrically programmable drug delivery in a diabetic wound healing electronic patch, *J. Controlled Release*, 2025, 113760.
30 H. Li, J. Cao, R. Wan, *et al.*, PEDOTs-based conductive hydrogels: design, fabrications, and applications, *Adv. Mater.*, 2025, **37**(7), 2415151.
31 B. Lu, H. Yuk, S. Lin, *et al.*, Pure PEDOT:PSS hydrogels, *Nat. Commun.*, 2019, **10**(1), 1043.
32 Y. Zhang and Y. Cui, Development of flexible and wearable temperature sensors based on PEDOT:PSS, *IEEE Trans. Electron Devices*, 2019, **66**(7), 3129–3133.
33 Y. Yin, C. Guo, W. Li, *et al.*, A super-elastic wearable strain sensor based on PU/CNTs yarns for human-motion detection, *Compos. Commun.*, 2024, **50**, 102017.
34 K. Zhao, Y. Zhao, J. Xu, *et al.*, Stretchable, adhesive and self-healing conductive hydrogels based on PEDOT:PSS-stabilized liquid metals for human motion detection, *Chem. Eng. J.*, 2024, **494**, 152971.
35 X. Chai, J. Tang, Y. Li, *et al.*, Highly stretchable and stimulus-free self-healing hydrogels with multiple signal detection performance for self-powered wearable temperature sensors, *ACS Appl. Mater. Interfaces*, 2023, **15**(14), 18262–18271.
36 D. Shin, Y. Lee, M. Sasaki, *et al.*, Violation of Ohm's law in a Weyl metal [A hallmark of the Weyl metal state: Breakdown of Ohm's law], *Nat. Mater.*, 2017, **16**(11), 1096–1099.
37 J. R. Macdonald, W. B. Johnson and I. D. Raistrick, *et al.*, *Impedance Spectroscopy: Theory, Experiment, and applications[M]*, John Wiley & Sons, 2018.
38 D. ASTM, *Standard Test Method for Water Absorption of plastics[J]*, ASTM, D570-98, 2010.
39 E. N. ISO, *37: 2017; Rubber, Vulcanized or Thermoplastic—Determination of Tensile Stress-Strain Properties[J]*, ISO International Organization for Standardization, Geneva, Switzerland, 2017.
40 M. Amjadi, K. U. Kyung, I. Park, *et al.*, Stretchable, skin-mountable, and wearable strain sensors and their potential applications: a review, *Adv. Funct. Mater.*, 2016, **26**(11), 1678–1698.
41 Y. Su, C. Ma, J. Chen, *et al.*, Printable, highly sensitive flexible temperature sensors for human body temperature monitoring: a review, *Nanoscale Res. Lett.*, 2020, **15**(1), 200.
42 J. Zheng, J. Zhou, Y. Zhao, *et al.*, A Low-Cost Hydrogel Electrode for Multifunctional Sensing: Strain, Temperature, and Electrophysiology, *Biosensors*, 2025, **15**(3), 177.
43 M. Jia and J. Zhang, Thermoresponsive PEDOT:PSS/PNIPAM conductive hydrogels as wearable resistive sensors for breathing pattern detection, *Polym. J.*, 2022, **54**(6), 793–801.
44 R. Ricciardi, G. Mangiapia, F. Lo Celso, *et al.*, Structural organization of poly (vinyl alcohol) hydrogels obtained by freezing and thawing techniques: A SANS study, *Chem. Mater.*, 2005, **17**(5), 1183–1189.
45 Y. C. Hsiao, L. C. Lee, Y. T. Lin, *et al.*, Stretchable polyvinyl alcohol and sodium alginate double network ionic hydrogels for low-grade heat harvesting with ultrahigh thermopower, *Mater. Today Energy*, 2023, **37**, 101383.
46 R. Zhang, Q. Fu, K. Zhou, *et al.*, Ultra stretchable, tough and self-healable poly (acrylic acid) hydrogels cross-linked by self-enhanced high-density hydrogen bonds, *Polymer*, 2020, **199**, 122603.
47 C. Shao, H. Chang, M. Wang, *et al.*, High-strength, tough, and self-healing nanocomposite physical hydrogels based on the synergistic effects of dynamic hydrogen bond and dual coordination bonds, *ACS Appl. Mater. Interfaces*, 2017, **9**(34), 28305–28318.
48 B. Kim and N. A. Peppas, Complexation phenomena in pH-responsive copolymer networks with pendent saccharides, *Macromolecules*, 2002, **35**(25), 9545–9550.
49 P. Li, H. Wang, Z. Ju, *et al.*, Ti3C2T x MXene-and Sulfuric Acid-Treated Double-Network Hydrogel with Ultralow Conductive Filler Content for Stretchable Electromagnetic Interference Shielding, *ACS Nano*, 2024, **18**(4), 2906–2916.
50 X. Liu, Z. Wu, D. Jiang, *et al.*, A highly stretchable, sensing durability, transparent, and environmentally stable ion conducting hydrogel strain sensor built by interpenetrating Ca2+-SA and glycerol-PVA double physically cross-linked networks, *Adv. Compos. Hybrid Mater.*, 2022, **5**(3), 1712–1729.
51 Y. Yin, C. Guo, W. Li, *et al.*, A super-elastic wearable strain sensor based on PU/CNTs yarns for human-motion detection, *Compos. Commun.*, 2024, **50**, 102017.
52 Y. Yin, C. Guo, Q. Mu, *et al.*, Dual-sensing nano-yarns for real-time pH and temperature monitoring in smart textiles, *Chem. Eng. J.*, 2024, **500**, 157115.
53 J. Yu, F. Tian, W. Wang, *et al.*, Design of highly conductive, intrinsically stretchable, and 3D printable PEDOT:PSS hydrogels *via* PSS-chain engineering for bioelectronics, *Chem. Mater.*, 2023, **35**(15), 5936–5944.

Open Access Article. Published on 02 January 2026. Downloaded on 6/16/2026 2:40:19 AM.
This article is licensed under a Creative Commons Attribution-NonCommercial 3.0 Unported Licence.

54 Q. Zhao, J. Liu, Z. Wu, *et al.*, Robust PEDOT:PSS-based hydrogel for highly efficient interfacial solar water purification, *Chem. Eng. J.*, 2022, **442**, 136284.
55 Z. Hou, Y. Li, D. Zhang, *et al.*, Tough Hydrogel Reinforced by Meta-Aramid Nanofibers for Flexible Sensors, *Polymers*, 2025, **17**(16), 2179.
56 Z. Deng, L. Shen, Q. Cheng, *et al.*, Anti-Swelling Antibacterial Hydrogels Based on Electrostatic Repulsion and Hydrophobic Interactions for Human Motion Sensing, *J. Funct. Biomater.*, 2025, **16**(9), 346.
57 G. Zeng, N. Yi, Q. Guo, *et al.*, Poly (Vinyl Alcohol)–Carbon Nanotube Self- Adhesive Hydrogels for Wearable Strain Sensors, *Polymers*, 2025, **17**(16), 2249.
58 S. Shinde and H. E. Lee, Wearable Strain Sensors *via* Tough and Conductive Hydrogel-Based MoS 2 Composites for Real-Time Motion Tracking, *ACS Omega*, 2025, DOI: 10.1021/acsomega.5c03752.
59 J. Zhuang, X. Zhang, W. Jin, *et al.*, Conductive, self-healing and adhesive cellulose nanofibers-based hydrogels as wearable strain sensors and supercapacitors, *Ind. Crops Prod.*, 2025, **225**, 120547.
60 J. Wei, R. Wang, F. Pan, *et al.*, Polyvinyl alcohol/graphene oxide conductive hydrogels *via* the synergy of freezing and salting out for strain sensors, *Sensors*, 2022, **22**(8), 3015.
61 Z. Zhang, G. Chen, Y. Xue, *et al.*, Fatigue-resistant conducting polymer hydrogels as strain sensor for underwater robotics, *Adv. Funct. Mater.*, 2023, **33**(42), 2305705.
62 X. Bao, Z. Chen, G. Nian, *et al.*, Unusually long polymers crosslinked by domains of physical bonds, *Nat. Commun.*, 2025, **16**(1), 4749.
63 Y. Zhu, D. Yao, X. Gao, *et al.*, Recyclable bimodal polyvinyl alcohol/PEDOT:PSS hydrogel sensors for highly sensitive strain and temperature sensing, *ACS Appl. Mater. Interfaces*, 2024, **16**(25), 32466–32480.

© 2026 The Author(s). Published by the Royal Society of Chemistry